PAPER

Check for updates

Enhancement of thermoelectrical performance in Au-ion implanted V_2O_5 thin films

Bilal Ahmad,[*a] Ramcharan Meena,[b] Pawan Kumar,[c] Rizwan Ahmed,[a] Majid Hussain, [ID][d] Shafiq Maqbool Tantary[e] and K. Asokan [ID][b]

The present study reports an enhancement of thermoelectric performance in Au ion implanted V_2O_5 thin films. Structural studies reveal the formation of nanocrystalline Au clusters in the Au ion implanted V_2O_5 thin films and some reduction of V_2O_5 phase into VO_2 phase due to the defects created by Au ion implantation. The electrical resistivity (ρ) of thin films is decreased by about a factor of 4 upon Au ion implantation, but the magnitude of the Seebeck coefficient $|S|$ decreases from 477.90 to 343.11 $\mu V\ K^{-1}$, and results in a significant increase of the power factor (PF). Engineering of the electronic density of states (DOS) and the energy filtering mechanism (EFM) are two different approaches that can improve the PF. However, a successful combination of these two methods is elusive. The present study demonstrates that the PF of Au implanted V_2O_5 thin films can be significantly promoted by both these effects. Simultaneous resonant distortions in DOS and EFM result in the enhancement in PF from 1.18×10^{-8} to 3.51×10^{-5}. This study may pave a way to prepare high-performance oxide based thermoelectric devices.

1. Introduction

Thermoelectric (TE) materials have attracted a great deal attention in recent years due to their ability to convert heat directly into electricity.[1,2] The conversion efficiency of a thermoelectric material is described by the figure of merit, ZT, defined as: $ZT = (S^2\sigma/\kappa)\ T = S^2\sigma T/(\kappa_e + \kappa_l)$, where σ is the electrical conductivity, S is the Seebeck coefficient, T is the absolute temperature, and κ is the total thermal conductivity including the contributions from electrons (κ_e) and lattice (κ_l).[3–6] Generally, high ZT needs a large power factor (PF $= S^2\sigma$), a low κ, or both. Both Bi_2Te_3 and PbTe are conventional thermoelectric materials that have high ZT, and have been commonly utilized in bulk forms.[7–9] In spite of their better thermoelectric properties in the bulk form, there are numerous difficulties in utilizing them in thin film forms for high temperature applications due to structural degradation and oxidation. For example, PbTe thin films change their thermoelectric properties through surface oxidation,[10] and $(Bi, Sb)_2(Te, Se)_3$ hot junctions suffer from increased resistance due to oxidation above 260 °C.[11] Oxides are naturally advantageous in their use at high temperatures and thus, a number of oxide systems have been investigated

recently.[12,13] Present study focuses on the properties of vanadium pentaoxide (V_2O_5) thin films as a thermoelectric device material.

The V_2O_5 has highest oxidation state in the V–O system and consequently the most stable one among these vanadium oxides with wide optical bandgap $\sim$2.24 eV.[14,15] It has a lamellar, or sheet like structure.[16] It is a distorted orthorhombic structure, and this deformation creates its sheet formation. These properties make V_2O_5 thin films a suitable candidate for scientific, industrial and technological applications, including catalytic material in gas sensors,[17,18] as a dielectric constituent material in super capacitors,[19] as a high capacity storage medium and as a cathode in Li-ion batteries,[20] or as a thermoresistive material in thermal infrared detectors.[21] Metal to insulator transition (MIT) at $\sim$280 °C in V_2O_5 by lattice distortion and a structural inhomogeneity due to the vanadyl-oxygen vacancies reported recently,[22–24] makes V_2O_5 a promising material for thermoelectric devices. In the insulating phase V_2O_5 possesses practically good value of S.[25,26] However, due to its relatively large bandgap, electron hopping is dominant transport processes where it accompanies lattice distortion, bearing small polaron hopping conduction. The V ions in V_2O_5 exist in the oxidation states of V^{4+} or V^{5+}, and the V^{4+} population is essentially equivalent to the small polaron population. The low concentration of the small polarons in V_2O_5 comes from the unintentional dopants and/or oxygen vacancies. Further, small polaron hopping materials tend to have low charge carrier mobility (μ).[27] Both the small number of polarons and low μ reveal the low σ of V_2O_5 that results small PF and ZT, thus making the material incompatible for any practical

[a]*Department of Physics, National Institute of Technology, Srinagar, J&K – 190006, India. E-mail: contactbilal1@gmail.com*

[b]*Materials Science Division, Inter University Accelerator Centre, New Delhi – 110067, India*

[c]*Department of Physics, Kurukshetra University, Kurukshetra, Haryana – 136119, India*

[d]*School of Material Science and Engineering, Tsinghua University, 100084, China*

[e]*Department of Physics, Govt. Degree College Sopore, J&K – 193201, India*

thermoelectric applications. Since V_2O_5 is a non-toxic abundant material[28] found in several mineral resources[29] there is a significant motivation to improve its σ, to acquire large power factor (PF) and better thermoelectric figures of merit (ZT), thus removing the impediment towards its extensive use for thermoelectric applications. Recently, the Density Functional Theory (DFT) simulations have predicted that controlled doping of V_2O_5 with metal elements can improve the PF due to a larger enhancement in electrical conductivity.[12] Recent studies have shown the enhancement primarily from physical–chemical interactions at the interface between the oxide and metal nanoparticles.[9,30,31] Metal like Ag ion is noble metal that is known to form nanoclusters when implanted in materials.[9,30] Similarly, Au nanoparticles is expected to provide evidence to suggest that the enhanced active site is the interface between the two metals. These also possess significant amount of free electrons that are likely to modify the electrical and thermal properties of these oxides leading to significant enhancement in S. These results have also been confirmed experimentally, for example, Na alloying has been shown to lead to a significant enhancement of the PF from 10^{-8} W K^{-2} m^{-1} to 10^{-5} W K^{-2} m^{-1}.[31] In this communication, we report the effect of Au ion implantation on thermoelectrical performance of V_2O_5 thin films.

2. Experimental details

Thin films of V_2O_5 were fabricated on quartz substrates by inorganic sol gel with spin coater. 0.3 grams of V_2O_5 (Sigma Aldrich, purity >99.9%) was dissolved in 30 ml, 30% hydrogen peroxide H_2O_2 (Sigma Aldrich) solution at room temperature with vigorous stirring using a magnetic stirrer till clear yellow solution is formed. This yellow solution was then heated at 60 °C on hot plate magnetic stirrer with continuous stirring to evolve excess oxygen by decomposition of H_2O_2 until the solution turned into red brown viscous gel. The overall mechanism is given in reactions as follows:[32]

$$V_2O_5 + 2H_2O_2 \rightarrow 2HVO_4 + H_2O$$

$$2HVO_4 + (n-1)H_2O \rightarrow V_2O_5 \cdot nH_2O + O_2 + H_2O$$
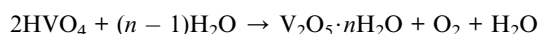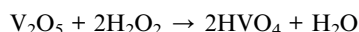
After aging for 24 hours, the V_2O_5 gel was accessible for coating and spin coater (SpinNXG-P1: made by Apex Instruments, India) was used to fabricate thin films on the quartz substrates. Before deposition, substrates were cleaned in dilute sulfuric acid for 45 minutes and then thoroughly rinsed in ethanol, acetone and de-ionized water subsequently. Ten successive coatings of V_2O_5 gel were performed on each substrate with each coating at the rate of 3000 rpm for 30 seconds and after each coating the films were dried at 80 °C for 20 minutes. Finally these V_2O_5 gel films were crystallized by annealing at 450 °C for 4 hours in the ambient atmosphere in programmable tubular furnace (Nabertherm GmbH Tube furnace: RHTC80) with heating and cooling rate of 3 °C per minute. These crystallized films were then vertically exposed to Au^- ion beam with energy 100 keV, at various ion fluences: 5×10^{15} ions per cm^2, 1×10^{16} ions per

cm^2 and 5×10^{16} ions per cm^2 using Negative Ion Facility at Inter-University Accelerator Centre (IUAC), New Delhi. The implantation was carried out at room temperature and pressure was maintained at 10^{-6} torr. For uniform implantation, the focused beam was allowed to scan over an area of 1×1 cm^2. After implantation the pristine and ion implanted films were again annealed in the ambient atmosphere for 1 hour at 400 °C. For convenience hereafter, the pristine as-deposited V_2O_5 thin films will be referred as P and the films implanted by Au ions at the ion fluences 5×10^{15}, 1×10^{16} and 5×10^{16} as I_{5E15}, I_{1E16} and I_{5E16} respectively. X-ray diffraction (XRD) measurements at room temperature in the 2θ range of 15–50° was performed to identify the crystalline phases and structure of the films using a Bruker D8 advance diffractometer with Cu Kα (0.15406 nm) X-ray source at a scan speed of 0.5° per min. Raman spectroscopy was performed using an Invia microRaman setup from Renishaw. The Ar ion laser with wavelength 488 nm, power 5 mW and exposure time of 40 seconds, was used in the Raman measurement. The Hall effect measurement was carried out by Ecopia HMS-3000 Hall Measurement System at room temperature to evaluate charge carrier density and mobility. The electrical resistivity (ρ) and thermoelectric power (S) of the films were measured in the temperature range from 300 to 400 K using DC standard four probe technique and bridge method,[33] respectively. The thickness was ~300 nm with the roughness typically in the order of ~30 nm. Since all the samples were grown under identical conditions by spin coating and ion implantation was performed after complete annealing of samples, the thickness, roughness etc. of all the samples are similar. The set up mentioned in ref. 33 was used for thermopower measurement and hence the error in the measurement is within 3%. The Hall effect measurements were done 4 times and average value is used for discussion.

3. Results and discussions

3.1. Structural studies

The typical XRD patterns and Raman spectra for P, I_{5E15}, I_{1E16} and I_{5E16} are shown in Fig. 1(a) and (b). The peaks at 20.27°, 26.22° and 41.25°, correspond to reflections from (001), (110) and (002) planes (see Fig. 1(a)) of the polycrystalline orthorhombic V_2O_5 phase (Pmmn space group symmetry, D_{2h} point group) with lattice constants $a = 11.51$ Å, $b = 3.56$ Å and $c = 4.37$ Å [JCPDS file no. #41-1426]. Absence of any other peak corresponds to any impurity or any other oxide of V in P indicates phase purity of pristine specimen. Large intensity of (001) peak at $2\theta = 20.27°$ suggests a preferential growth along the (001) planes. The V_2O_5 crystal structure projected along (001) lattice plane is depicted by the geometrical diagram with its characteristics interatomic distance is shown in Fig. 1(c).[34] The V atom and the three inequivalent oxygen positions O_3 (bridge), O_1 (vanadyl) and O_2 (chain) are shown along with the bonds between the V and the nearest neighbouring oxygen atoms. In the y direction, the linear chain oxygen atoms are linked together with V atoms and in the x direction, the V atoms are connected by the bridge oxygen atoms. The bond length of V and O atoms are 1.779 Å (V–O_3), 1.878 Å (V–O_2(2)) and 2.021 Å (V–O_2(1)). The vanadyl oxygens are positioned above and below the V atoms creating variable
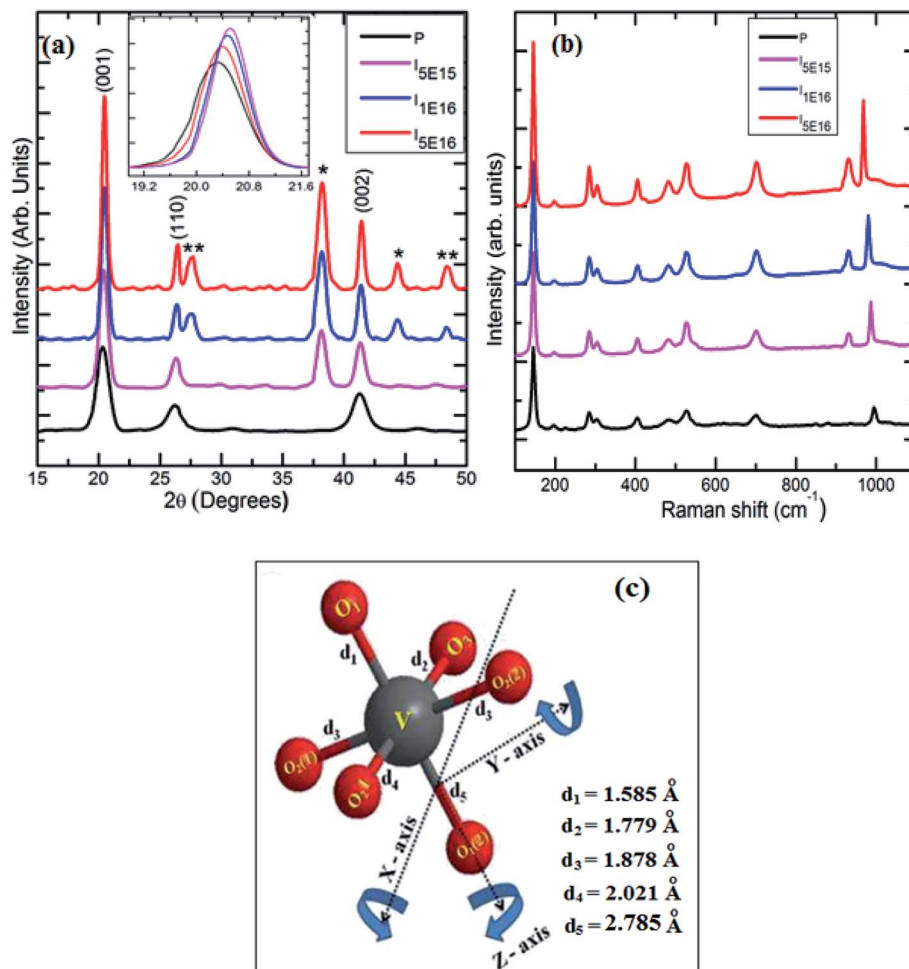
Fig. 1 (a) XRD spectra of pristine and ion implanted specimens. The '*' indexed peaks corresponds to face centered cubic Au phase and the '**' indexed peaks corresponds to VO_2 monoclinic phase. (b) Raman spectra of pristine and ion implanted specimens. (c) Geometrical 3D view of V_2O_5 structure with the characteristic interatomic distances.[34]

V–O distances the shortest (1.585 Å) and longest (2.785 Å) in this structure along the z direction. This structure can be described as a ladder structure with the legs running along y direction with rungs along x direction.[35] Each V atom and its five nearest O neighbours create VO_5 pyramids which split their corners within the ladder and their edges between neighbouring ladders. The resulting layers are stacked along the c direction and the V is in fact shifted out of the base plane of the pyramid toward the vanadyl oxygen.[35] The peaks at 38.15° in I_{5E15}, I_{1E16} & I_{5E16} and at 44.35° in I_{1E16}, I_{5E16} correspond to (111) and (200) reflections respectively from face centered cubic Au phase (JCPDS card no 021095, space group $Fm3m$). The broadness of Au peaks in the diffraction patterns indicates clearly the formation of nano-crystalline Au clusters in the Au ion implanted V_2O_5 thin films and increase in intensity of these peaks indicates that density of size of Au nanoparticles increases with increase in ion fluences. This indicates most of Au in the film is separated particles.

The peak appearing at 27.43°, and 48.44° in I_{1E16} and I_{5E16} correspond to reflections from (011), and (300) planes of the monoclinic VO_2 phase [JCPDS card no 82-0661, space group $P2_1/C$]. Increase in the intensity of these peaks with ion fluence

signifies reduction of V_2O_5 into VO_2 and thus increase in V^{4+} population upon ion implantation. Inset of the Fig. 1(a) presents magnified view of V_2O_5 (001) peak. An increase in peak intensity, decrease in full width at half maxima (FWHM), and slight shift towards higher 2θ are noticed as shown in the inset with ion implantation demonstrating the decrease of adjacent interplanar (d) spacing and the improvement in crystalline nature of V_2O_5 films with ion implantation. The average crystallite size (D) of the V_2O_5 is estimated from V_2O_5 (001) reflection plane by using the Scherrer's formula.[36] The microstrain 'ε' is calculated from the relation:[36]

$$\delta = \frac{\beta \cos \theta}{\lambda} = \frac{1}{D} + \frac{\varepsilon \sin \theta}{\lambda}, \tag{1}$$

The dislocation density (δ) defined as the length of dislocation lines per unit volume of the crystal and to be determined from the crystallite size (D) by the relation:[36]

$$\delta = \frac{n}{D^2}, \tag{2}$$

where n is an integer and $n = 1$ gives minimum dislocation density. The number of crystallites/area (N) is calculated using the formula:[36]

$$N = \frac{t}{D^2},\qquad(3)$$

where t is film thickness. The texture coefficient corresponding to [hkl] miller plane ($T_c(hkl)$) is calculated from the formula:[36]

$$T_c(hkl) = \frac{I(hkl)/I_0(hkl)}{\sum\limits_{n-1}^{n} I(hkl)/I_0(hkl)}\qquad(4)$$

where $I(hkl)$ is the measured relative intensity of a plane (hkl), $I_0(hkl)$ is the standard relative intensity of the plane (hkl) taken from the JCPDS card, n is the number of reflections. Stacking fault probability was calculated from the formula,

$$\alpha = \left(\frac{2\pi^2}{45\sqrt{3}}\right)\left(\frac{\Delta(2\theta)}{\tan\theta}\right),\qquad(5)$$

Table 1 shows the variation of microstructural parameters such as crystallite size, interplanar spacing, microstrain, dislocation density, number of crystallites, texture coefficient, and stacking fault probability for pristine and Au ion implanted V_2O_5 thin films estimated from the XRD analysis of the samples at the main intensity peak of (001) of V_2O_5. It is evident from Table 1 that D increase, whereas d, and ε decrease with ion implantation. The increase in grain size in implanted films may be due to the diffusion of Au-ions into V_2O_5, which provide nucleation site for grain growth and hence increases the crystallinity.[20] The microstrain values of P, I_{5E15}, I_{1E16} and I_{5E16} are found to be 0.25, 0.22, 0.19, and 0.18 nm respectively. The evaluated microstrain values are inversely proportional to the crystallite size of the films. This may be due to an enhancement of internal microstrain with decrease in crystallite size of the films.[37] Dislocation density, number of crystallites and texture coefficient decrease with increase in ion fluence due to increase in grain size. Fault probability shows irregular variation first decrease, then increase and then again decrease.

Raman spectroscopy is known to be a very useful technique used to characterize the structural order–disorder degree at short range and crystallinity of oxide materials. Fig. 1(b) displays the Raman spectra in the wavelength range of 100–1100 cm^{-1} of P, I_{5E15}, I_{1E16} and I_{5E16}. Raman spectrum of P matches with Stokes lines assigned to orthorhombic V_2O_5 phase.[38,39] Table 2 presents the modes assigned to the peaks

Table 2 Raman peaks observed in pristine samples along with assignment of bands

Peak	Band assigned
144	Skeleton bent vibration (B_{3g} species)
196	V=O bending mode (A_g mode)
284	V=O bending mode (B_{2g} mode)
304	R_x liberation mode (A_g species)
405	V=O bending mode (A_g mode)
481	V–O–V bending vibration
527	Triply coordinated oxygen (V_3–O) (A_g species)
701	Doubly coordinated oxygen (V_2–O) stretching mode (B_{2g} and B_{3g} species)
995	Terminal oxygen (V=O) stretching mode

observed in the pristine samples. The most intense peak present at 144 cm^{-1} is attributed to skeleton bent vibration (B_{3g}), while peaks located at 196, 284 and 405 cm^{-1} are corresponding to the bending vibrations of V=O bonds. The peaks located at 481 and 304 cm^{-1} are assigned to the bending vibrations of the bridging V–O–V (doubly coordinated oxygen) and V–O (triply coordinated oxygen) bonds, respectively. The peak at 527 cm^{-1} is attributed to the triply coordinated oxygen atom (V_3–O) stretching mode, aroused from the edge-shared oxygen atoms common to three VO_5 pyramids. The peak positioned at 701 cm^{-1} is attributed to the doubly coordinated oxygen (V_2–O) asymmetric stretching mode which originates from corner shared oxygen common to two VO_5 pyramids. The high frequency peaks at 995 cm^{-1} corresponds to the stretching mode of terminal oxygen (V=O) which arises from an unshared oxygen. No other peaks representing secondary phases of V and O were observed in Raman spectra of P that ascertains phase purity of pristine samples. The high frequency Raman peak at 995 cm^{-1} that corresponds to the stretching mode of terminal oxygen (V=O) gives the structural quality of the films and can be ascribed to the stretching mode related to the A_g symmetry vibrations of the of the shortest V and O bond, which is V=O. Unlike the other O atoms this atom is strongly bonded to only one V atom and for this reason is called terminal O.[40] The frequency shift of this mode measures the deviations from stoichiometry. The frequency shift to lower values of this mode is due to softening of the V^{5+}=O bond in oxygen deficient V_2O_5 films, resulting from vacancies created by removing O_V, with some of the V^{5+} reduced to V^{4+} in order to balance the charge. Negligible frequency shift of this mode manifests good stoichiometry of pristine samples. The shift in the peak position of

Table 1 Microstructural parameters of Au ion implanted V_2O_5 thin films calculated from XRD analysis

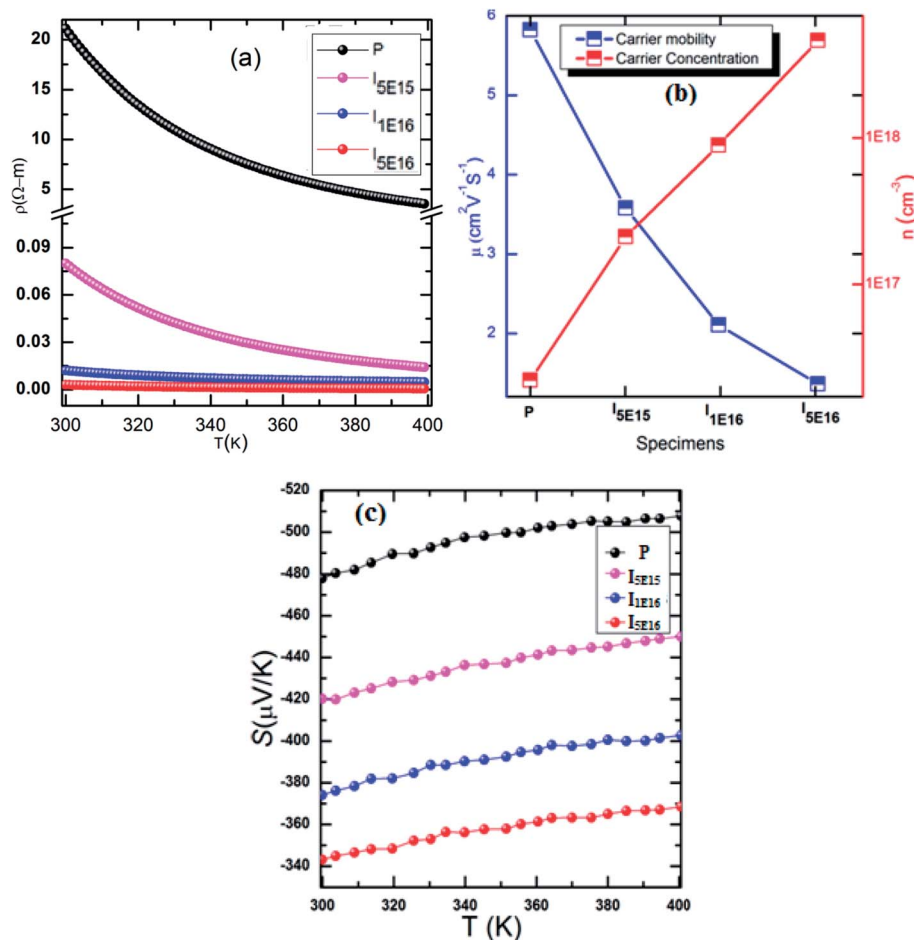| Sample	D (nm)	d (Å)	$\varepsilon \times 10^{-2}$ (lines^{-2} m^{-4})	$\delta \times 10^{15}$ (lines m^{-2})	$N \times 10^4$ (crystallites m^{-2})	T_c	α
P	10.42	4.37	0.25	1.31	54	1.32	0.023
I_{5E15}	12.04	4.35	0.22	1.03	37	1.48	0.015
I_{1E16}	15.56	4.32	0.19	0.84	28	1.63	0.029
I_{5E16}	16.13	4.33	0.18	0.78	25	1.68	0.027

Fig. 2 (a) Electrical resistivity verses temperature of specimens. (b) Carrier density and carrier mobility of samples. (c) Seebeck coefficient as a function of temperature of samples.

986, 980, and 968 cm^{-1} for I_{5E15}, I_{1E16} and I_{5E16} respectively indicates that some reduction of V^{5+} to V^{4+} upon Au ion implantation in V$_2$O$_5$ thin films. This is also evident as a peak corresponding to V^{4+}=O near 932 cm^{-1} is observed in ion beam implanted V$_2$O$_5$ thin films.[41] Enhancement in peak intensities in ion implanted thin films indicates that the crystallinity increases with ion implantation. Absence of peak at 850 cm^{-1} indicates that the films are not hydrated (V$_2$O$_5$·H$_2$O) which is normally observed in V$_2$O$_5$ as contaminant.[42] The presence of peak at 141 cm^{-1} and 194 cm^{-1} in P, I_{5E15}, I_{1E16} and I_{5E16} confirms that layer-like structure is retained after ion implantation.[39] During ion implantation oxygen vacancies are created. Such vacancies result in reducing the oxidation state of V and

hence some of the V$_2$O$_5$ reduces into VO$_2$. Similar results of reduction of oxides of Fe, Co, Ti and Nb by low-energy ion bombardment have been reported by Choudhury et al.[43]

3.2. Electrical and thermo electrical studies

The temperature dependence of electrical resistivity (ρ), for P, I_{5E15}, I_{1E16}, and I_{5E16}, in the temperature range 300–400 K is shown in Fig. 2(a). Decrease in ρ with temperature indicates that the samples exhibit semiconducting behavior in this temperature range. Further, in the entire temperature range the resistivity decreases in the order: $P > I_{5E15} > I_{1E16} > I_{5E16}$. The resistivity of P, I_{5E15}, I_{1E16}, and I_{5E16} at room temperature are 21.101, 0.080, 0.012, and 0.003 (Ω m) respectively (see Table 3).

Table 3 Room temperature electrical resistivity, carrier concentration, carrier mobility, Seebeck coefficient, power factor, band gap and effective mass of for the P, I_{5E15}, I_{1E16}, and I_{5E16} samples

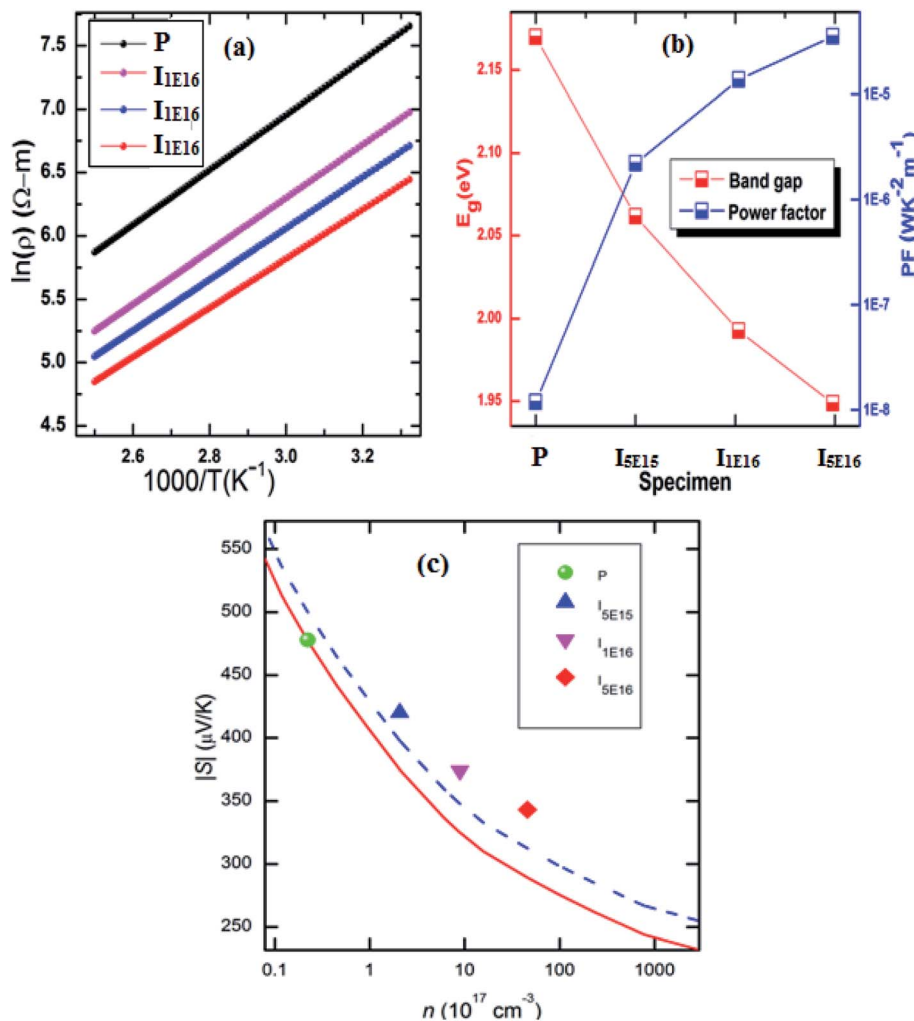| Specimen	ρ (Ω m)	n (cm^{-3})	μ (cm^2 V^{-1} s^{-1})	S (μV K^{-1})	PF (W K^{-2} m^{-1})	E_a (eV)	m^*
P	21.101	2.20×10^{16}	5.82	−477.93	1.08×10^{-8}	2.17	$1.52m_e$
I_{5E15}	0.080	2.08×10^{17}	3.57	−420.15	2.21×10^{-6}	2.06	$2.18m_e$
I_{1E16}	0.012	8.91×10^{17}	2.11	−374.17	1.40×10^{-5}	1.99	$2.68m_e$
I_{5E16}	0.003	4.60×10^{18}	1.36	−343.11	3.90×10^{-5}	1.95	$3.06m_e$

Fig. 3 (a) ln(ρ) *vs.* 1000/T plot. (b) The calculated activation energy and power factor of specimens. (c) Variation of Seebeck coefficient with carrier concentration. Red solid line represents the carrier concentration dependence of S without any secondary effect. Blue Dashed represents the carrier concentration dependence of S considering only electronic DOS.

Fig. 2(b) shows the carrier concentration (n) and mobility (μ) of the films measured at room temperature for specimens. The value of n increases rapidly with Au ion implantation and μ decreases due to the impurity scattering by implanted ions. The measured carrier concentrations are $\sim$2.20 $\times$ 10^{16} cm^{-3}, $\sim$2.08 $\times$ 10^{17} cm^{-3}, $\sim$8.91 $\times$ 10^{17} cm^{-3}, and $\sim$4.60 $\times$ 10^{18} cm^{-3} and carrier mobility are $\sim$5.82, $\sim$3.57, $\sim$2.11, and $\sim$1.36 for P, I_{5E15}, I_{1E16}, and I_{5E16}, respectively (Table 3). The decrease in ρ is attributed to the increased carrier concentration by Au ion implantation, despite of the slight decrease in Hall mobility. Iwanaga *et al.* investigated the effect of Na alloying in V$_2$O$_5$ and observed a significant enhancement of thermopower.[31] It was also demonstrated by them that increasing Na concentration increases the electrical conductivity by a factor of up to $\sim$104, whereas the S decreased only by a half and the power factor improved upto 350 times. Similarly Lourerio *et al.* observed that by Cr doping the thermoelectric properties are enhanced significantly.[13] Presence of nanograins in the films are responsible for an improvement of electrical and thermal properties.

Bala *et al.* also showed that addition of Au either by chemical addition or by ion implantation results in better properties in PbTe.[30,31] Present investigation is consistent with above results.

To further investigate the influence of Au ion implantation, the activation energy (E_a) was anticipated from the slope of linear fit of ln(ρ) *vs.* 1000/T curve (Fig. 3(a)) according to the Arrhenius formula:[44]

$$\rho = \rho_0 \exp(E_a/2K_b T) \qquad (6)$$

where ρ is the electrical resistivity and ρ_0 is a constant. The calculated values of E_a are 2.17, 2.06, 1.99 and 1.95 eV for the P, I_{5E15}, I_{1E16}, and I_{5E16} samples, respectively (Fig. 3(b)). It can thus be concluded that the activation energy decreases with Au content. This is consistent with the increase in carrier concentration and decrease in electrical resistivity.

The variations of thermoelectric power (S) of the specimens are shown in Fig. 2(c). Negative value S reflects dominant n-type conduction mechanism in the specimens. The temperature dependences of S shows that $|S|$ increase with temperature for

all the specimens. Further, $|S|$, decrease with ion implantation. The measured values of S for P, I_{5E15}, I_{1E16} and I_{5E16} films at room temperature are -477.93, -420.15, -374.17, and -343.11 μV K^{-1} respectively (Table 3). Large increase in electrical conductivity in comparison to small decrease in $|S|$ results an overall increase in power factor (PF $= S^2\sigma$). The PF of P, I_{5E15}, I_{1E16}, and I_{5E16} at room temperature are $\sim1.18 \times 10^{-8}$, $\sim2.21 \times 10^{-6}$, $\sim1.40 \times 10^{-5}$ and 3.51×10^{-5} W K^{-2} m^{-1} respectively. Generally, there is a tradeoff between the S and the σ since S and σ vary in a reciprocal way, and both the values are also dependent on each other with carrier density (n). Increasing n usually results in decrease in the S in accordance with increase in σ and thus prevents any enhancement in PF and ZT. However, in present work, there is only slight decrease in S with Au ion implantation of V$_2$O$_5$ thin films in spite of appreciable increase in σ by factor 10^4, leads to increase in PF. Since E_a for all the samples is larger than $3KT$ (75 meV) therefore all the samples belong to degenerated semiconductors. According to the Mott, the thermopower S of a degenerate semiconductor, can be expressed as:[45]

$$s = \frac{\pi^2}{3}\frac{K_b^2 T}{q}\left[\frac{\partial \ln(\sigma(E))}{\partial(E)}\right]_{E=E_f}$$

$$= \frac{\pi^2}{3}\frac{K_b^2 T}{q}\left[\frac{1}{n(E)}\frac{\partial n(E)}{\partial E} + \frac{1}{\mu}\frac{\partial \mu(E)}{\partial E}\right]_{E=E_f}, \quad (7)$$

where σ is the electrical conductivity, q is the carrier charge, $n(E)$ and $\mu(E)$ are energy dependent charge carrier density and carrier mobility, λ is the scattering parameter, K_b is the Boltzmann constant, m^* is the effective mass and E_f the Fermi energy. With the approximation of a free-electron gas and assuming an exponential dependence of the scattering parameter λ on the relaxation time τ, i.e. $\tau = \tau_0 E^{\lambda-1/2}$ (here τ_0 is an energy-independent constant), eqn (7) can be written as:

$$S \approx \frac{\pi^2 K_b^2 T}{3e}\left[\frac{D(E)}{n} + \frac{\lambda - \frac{1}{2}}{E}\right]_{E=E_f}. \quad (8)$$

Here $D(E)$ is the electronic density of states (DOS). Eqn (8) implies that at a given carrier concentration (n), S can be enhanced by either increasing $D(E)$, i.e. the electronic DOS at the Fermi level, or the scattering parameter λ that corresponds to the energy filtering mechanism (EFM).[14,46] The effective mass m^* is estimated based on the measured values of carrier concentration (n) and thermopower (S). Assuming a single parabolic band model with acoustic phonon scattering, m^* and S can be approximated by:[47,48]

$$m \approx \frac{h^2}{2K_b T}\left[\frac{n}{4\pi F_{1/2}(\eta)}\right]^{2/3} \quad (9)$$

$$S = \frac{K_b}{e}\left[\frac{(2+\lambda)F_{\lambda+1}(\eta)}{(1+\lambda)F_\lambda(\eta)} - \eta\right], \quad (10)$$

where K_b is the Boltzmann constant, h is the Planck constant, e is elementary charge, λ is a scattering parameter related to the energy dependence of the carrier scattering mechanism,

η ($=E_f/K_b T$) is the reduced Fermi level, and $F_j(\eta)$ is the Fermi integral of order j and is given by:

$$F_j(\eta) = \int_0^\infty \frac{x^j}{1 + \exp(x - \eta)}dx \quad (11)$$

According to Heremans et al., the scattering parameter λ of doped systems without inclusions (or secondary phase) is dominated by the acoustic modes and can be zeroed.[48,49] The calculated m^* for P, I_{5E15}, I_{1E16}, and I_{5E16} are $1.52m_e$, $2.18m_e$, $2.68m_e$ and $3.06m_e$, respectively (Table 3). The large effective mass of ion implanted samples in comparison to P specifies that there is strong resonant distortion of the electronic DOS around the Fermi level, since the DOS is directly related to effective mass m^* as:[50]

$$D(E) = \frac{4\pi(2m^*)^{3/2}E^{1/2}}{h^3} \quad (12)$$

Using formulae (11) and (12) and $m^* = 1.52m_e$ and $\lambda = 0$ for the P, one can plot the dependence of S on carrier concentration at 300 K (solid red line in Fig. 3(c)). Without resonant distortion of the electronic DOS, the thermopower S of Au implanted thin films should lie on the same line. However, it is found that S of I_{5E15}, I_{1E16}, and I_{5E16}, is ~45, ~49 and ~54 μV K^{-1} higher than the values of the solid red line, respectively (Fig. 3(c)), indicating strong electronic DOS resonant distortion effects. Further using the same formulae with and $m^* = 2.18m_e$; $2.68m_e$ and $3.06m_e$, and $\lambda = 0$, the thermopower S at 300 K for I_{5E15}, I_{1E16}, and I_{5E16} would be ~398, ~346, and 311 μV K^{-1} respectively and the method of extrapolating yields the blue dashed line in Fig. 3(C). Without energy filtering effect thermopower values of ion implanted V$_2$O$_5$ thin films should lie on this dotted blue line. But measured S values of I_{5E15}, I_{1E16}, and I_{5E16}, are ~23, 28, and 32 μV respectively, above the line, demonstrating that there is energy filtering effect in Au implanted thin films. It is known that ZT depends on PF and k. With implantation, the value of σ increases drastically because of large number of free electrons supplied by Au ions. Apart from this due to Au implantation, there is also nanostructuring that results due to Au clusters as evident from XRD. This contributes significantly for k_e and k_L which are components of k. Au and VO$_2$ nanograins gets formed in Au ion implanted thin films as discussed in structural studies acts as nanoinclusions in the matrix of V$_2$O$_5$, leading to the formation of heterojunction potential barriers at the phase boundary and these potential barriers act as additional scattering centers giving rise to the EFM that contributes to the large enhancement of S.[51] Above behaviours have been understood on the basis of combined effects of resonant distortion of the electronic DOS, and carrier energy filtering.

4. Conclusions

Thin films of V$_2$O$_5$ were fabricated on quartz substrates by simple inorganic sol-gel method and 100 keV Au$^-$ ions at various fluences were implanted in these films. The structural studies show the presence of Au and VO$_2$ nanograins in the

matrix of V_2O_5 upon ion implantation and these nanograins acts as nanoinculsions. Electrical transport studies exhibit that with Au ion implantation, the Seebeck coefficient decreases slightly in spite of appreciable increase in electrical conductivity by factor 10^4, that results in increase in power factor. This demonstrates that Au ion implantation improved the thermo-electric properties of the V_2O_5 thin films. The origin of such behaviour of Seebeck coefficient results from the combination of resonant distortion of the electronic DOS in the Au ion implanted V_2O_5 thin films and intensified by energy filtering at the heterojunction potential barriers formed due to Au and VO_2 nanoinculsions. These findings will be helpful to design high-performance oxide thermoelectric devices.

Conflicts of interest

There are no conflicts to declare.

Acknowledgements

References

1 S. G. Jeffrey and E. S. Toberer, Complex thermoelectric materials, *Nat. Mater.*, 2008, **7**(2), 105–114.

2 L.-D. Zhao, *et al.*, Ultralow thermal conductivity and high thermoelectric figure of merit in SnSe crystals, *Nature*, 2014, **508**(7496), 373–377.

3 Y. Pei, *et al.*, Convergence of electronic bands for high performance bulk thermoelectrics, *Nature*, 2011, **473**(7345), 66–69.

4 K. Biswas, *et al.*, High-performance bulk thermoelectrics with all-scale hierarchical architectures, *Nature*, 2012, **489**(7416), 414–418.

5 R. Venkatasubramanian, *et al.*, Thin-film thermoelectric devices with high room-temperature figures of merit, *Nature*, 2001, **413**(6856), 597–602.

6 K. F. Hsu, *et al.*, Cubic AgPb(m)SbTe(2 + m): bulk thermoelectric materials with high figure of merit, *Science*, 2004, **303**(5659), 818–821.

7 H. J. Goldsmid, The electrical conductivity and thermoelectric power of bismuth telluride, *Proceedings of the Physical Society*, 1958, **71**(4), 633.

8 Y. Gelbstein, Z. Dashevsky and M. P. Dariel, High performance n-type PbTe-based materials for thermoelectric applications, *Phys. B*, 2005, **363**(1), 196–205.

9 M. Bala, *et al.*, Enhancement of thermoelectric power of PbTe:Ag nanocomposite thin films, *RSC Adv.*, 2015, **5**, 25887–25895.

10 E. I. Rogacheva, S. G. Lyubchenko and M. S. Dresselhaus, Effect of oxidation on thickness dependencies of thermoelectric properties in PbTe/mica thin films, *Thin Solid Films*, 2005, **476.2**, 391–395.

11 C. Huang and A. Christou, Diffusion controlled degradation analysis of high temperature (Bi, Sb)2 (Te, Se) 3 semiconductor thermoelectric power modules, *Mater. Sci. Eng., B*, 1995, **29**(1–3), 233–236.

12 Y. Chumakov, S. Y. Xiong, J. R. Santos, I. Ferreira, K. Termentzidis, A. Pokropivny, P. Cortona and S. Volz, *J. Electron. Mater.*, 2012, **42**, 1597–1603.

13 J. Loureiro, *et al.*, Nanostructured p-type Cr/V_2O_5 thin films with boosted thermoelectric properties, *J. Mater. Chem. A*, 2014, **2**, 6456.

14 F. J. Morin, Oxides which show a metal-to-insulator transition at the Neel temperature, *Phys. Rev. Lett.*, 1959, **3**(1), 34.

15 R. L. Smith, *et al.*, A scanning probe microscopy study of the (001) surfaces of V_2O_5 and V_6O_{13}, *Surf. Sci.*, 1996, **367**(1), 87–95.

16 K. Sieradzka, *et al.*, Structural and optical properties of vanadium oxides prepared by microwave-assisted reactive magnetron sputtering, *Opt. Appl.*, 2011, **41**(2), 463–469.

17 N. Izu, *et al.*, Application of V_2O_5/WO_3/TiO_2 for resistive-type SO_2 sensors, *Sensors*, 2011, **11**(3), 2982–2991.

18 K. Hermann, *et al.*, Ab initio density functional theory studies of hydrogen adsorption at the V_2O_5 (010) surface, *Phys. Status Solidi A*, 1999, **173**(1), 195–208.

19 Y. Yang, *et al.*, Vertically aligned mixed V_2O_5–TiO_2 nanotube arrays for supercapacitor applications, *Chem. Commun.*, 2011, **47**(27), 7746–7748.

20 A.-M. Cao, *et al.*, Self-assembled vanadium pentoxide (V_2O_5) hollow microspheres from nanorods and their application in lithium-Ion batteries, *Angew. Chem., Int. Ed.*, 2005, **44**(28), 4391–4395.

21 P. W. Kruse, *Uncooled thermal imaging: arrays, systems, and applications*, SPIE press, 2001, vol. 51.

22 M. Kang, *et al.*, Metal-insulator transition without structural phase transition in V_2O_5 film, *Appl. Phys. Lett.*, 2011, **98**(13), 131907.

23 R.-P. Blum, *et al.*, Surface metal-insulator transition on a vanadium pentoxide (001) single crystal, *Phys. Rev. Lett.*, 2007, **99**(22), 226103.

24 A. L. Pergament, G. B. Stefanovich and A. A. Velichko, Oxide electronics and vanadium dioxide perspective: A review, *Journal on Selected Topics in Nano Electronics and Computing*, 2013, **1**(1), 24–43.

25 R. Santos, *et al.*, Thermoelectric properties of V_2O_5 thin films deposited by thermal evaporation, *Appl. Surf. Sci.*, 2013, **282**, 590–594.

26 D. K. Chakrabarty, D. Guha and A. B. Biswas, Electrical properties of vanadium pentoxide doped with lithium and sodium in the α-phase range, *J. Mater. Sci.*, 1976, **11**(7), 1347–1353.

27 P. Vaqueiro and A. V. Powell, Recent developments in nanostructured materials for high-performance thermoelectrics, *J. Mater. Chem.*, 2010, **20**(43), 9577–9584.

28 R. R. Moskalyk and A. M. Alfantazi, Processing of vanadium: a review, *Miner. Eng.*, 2003, **16**(9), 793–805.

29 K. Koumoto, I. Terasaki and R. Funahashi, Complex oxide materials for potential thermoelectric applications, *MRS Bull.*, 2006, **31**(03), 206–210.

30 M. Bala, *et al.*, Enhancement of thermoelectric power of PbTe thin films by Ag ion implantation, *J. Appl. Phys.*, 2017, **121**, 215301.

31 S. Iwanaga, *et al.*, Thermopower and electrical conductivity of sodium-doped V_2O_5 thin films, *J. Appl. Phys.*, 2007, **101**(12), 123709.

32 X. Ren, *et al.*, Preparation and electrochemical properties of V_2O_5 submicron-belts synthesized by a sol–gel H_2O_2 route, *J. Sol-Gel Sci. Technol.*, 2009, **51**(2), 133–138.

33 T. S. Tripathi, M. Bala and K. Asokan, An experimental setup for the simultaneous measurement of thermoelectric power of two samples from 77 K to 500 K, *Rev. Sci. Instrum.*, 2014, **85**(8), 085115.

34 H.-G. Bachmann, F. Ramadan Ahmed and W. H. Barnes, The crystal structure of vanadium pentoxide, *Z. Kristallog. – Cryst. Mater.*, 1961, **115**(1–6), 110–131.

35 S. Atzkern, *et al.*, Valence-band excitations in V_2O_5, *Phys. Rev. B: Condens. Matter Mater. Phys.*, 2000, **61**(19), 12792.

36 B. D. Cullity, in *Elements of X-ray Diffraction*, Addison-Wesley Publishing Inc, Massachusetts, U.S.A, 1956.

37 S. Thiagarajan, M. Thaiyan and R. Ganesan, Physical property exploration of highly oriented V_2O_5 thin films prepared by electron beam evaporation, *New J. Chem.*, 2015, **39**(12), 9471–9479.

38 R. Baddour-Hadjean, *et al.*, Lattice dynamics of β-V_2O_5: Raman spectroscopic insight into the atomistic structure of a high-pressure vanadium pentoxide polymorph, *Inorg. Chem.*, 2012, **51**(5), 3194–3201.

39 B. A. Bhat, G. R. Khan and K. Asokan, Role of substrate effects on the morphological, structural, electrical and thermoelectrical properties of V_2O_5 thin films, *RSC Adv.*, 2015, **5**(65), 52602–52611.

40 P. Clauws, J. Broeckx and J. Vennik, Lattice Vibrations of V2O5. Calculation of Normal Vibrations in a Urey-Bradley Force Field, *Phys. Status Solidi B*, 1985, **131**(2), 459–473.

41 S.-H. Lee, *et al.*, Raman spectroscopic studies of amorphous vanadium oxide thin films, *Solid State Ionics*, 2003, **165**(1), 111–116.

42 X. Chen, *et al.*, Ozone-based atomic layer deposition of crystalline V_2O_5 films for high performance electrochemical energy storage, *Chem. Mater.*, 2012, **24**(7), 1255–1261.

43 T. Choudhury, *et al.*, Reduction of oxides of iron, cobalt, titanium and niobium by low-energy ion bombardment, *J. Phys. D: Appl. Phys.*, 1989, **22**, 1185–1195.

44 N. F. Mott and E. A. Davis, *Electronic process in non-crystalline materials*, Oxford University Press, 1971.

45 M. Jonson and G. D. Mahan, Mott's formula for the thermopower and the Wiedemann-Franz law, *Phys. Rev. B: Condens. Matter Mater. Phys.*, 1980, **21**(10), 4223.

46 T. Zou, *et al.*, Enhanced thermoelectric performance of β-Zn4Sb3 based nanocomposites through combined effects of density of states resonance and carrier energy filtering, *Sci. Rep.*, 2015, **5**, 17803.

47 H. Xie, *et al.*, Beneficial Contribution of Alloy Disorder to Electron and Phonon Transport in Half-Heusler Thermoelectric Materials, *Adv. Funct. Mater.*, 2013, **23**(41), 5123–5130.

48 T. Caillat, J.-P. Fleurial and A. Borshchevsky, Preparation and thermoelectric properties of semiconducting Zn4Sb3, *J. Phys. Chem. Solids*, 1997, **58**(7), 1119–1125.

49 J. P. Heremans, *et al.*, Enhancement of thermoelectric efficiency in PbTe by distortion of the electronic density of states, *Science*, 2008, **321**(5888), 554–557.

50 C. Kittel, *Introduction to solid state physics*, Wiley, New York, 8th edn, 2005, ch. 6, pp. 131–157.

51 X. H. Yang, *et al.*, Enhanced thermopower and energy filtering effect from synergetic scattering at heterojunction potentials in the thermoelectric composites with semiconducting nanoinclusions, *J. Alloys Compd.*, 2013, **558**, 203–211.